RSC Advances

PAPER

View Article Online
View Journal | View Issue

Cite this: *RSC Adv.*, 2023, **13**, 36130

A combined first principles and experimental approach to Bi_2WO_6†

Quazi Shafayat Hossain, [a] Sadiq Shahriyar Nishat, [b] Mohsina Sultana, [a] Tasnim Ahmed Mahi, [ac] Shahran Ahmed, [ad] M. N. I. Khan, [e] H. N. Das, [e] Muhammad Shahriar Bashar, [f] Umme Sarmeen Akhtar, [g] Sharmin Jahan, [h] Fariha Chowdhury, [i] Khandker Saadat Hossain, [j] Sazzad M. S. Imran [a] and Imtiaz Ahmed *[a]

Here we synthesized Bi_2WO_6 (BWO) using both solid-state reaction (SBWO) and hydrothermal (HBWO-U and HBWO-S) methods. The orthorhombic $Pca2_1$ phase purity in all samples is confirmed from Rietveld refinement of X-ray diffraction data, Raman spectroscopy, and Fourier transform infrared spectroscopy. The HBWO-U and HBWO-S morphology revealed rectangular, spherical, and rod-like features with an average particle size of 55 nm in field emission scanning electron micrographs. A high-resolution transmission electron micrograph showed spherical-shaped particles in the HBWO-U sample with an average diameter of ~10 nm. The diffuse reflectance-derived indirect electronic band gaps lie within the 2.79–3.23 eV range. The BWO electronic structure is successfully modeled by Hubbard interaction U_d and U_p corrected Perdew–Burke–Ernzerhof generalized gradient approximation GGA-PBE+U_d+U_p with van der Waals (vdW) force in effect. The optimized (U_d, U_p) values are further justified by tuning the Hartree–Fock (HF) exact-exchange mixing parameter α_{HF} from 25% in Heyd–Scuseria–Ernzerhof (HSE06) to 20% in the PBE-HF20% functional. Moreover, no inconsistencies were seen in the GGA-PBE+U_d+U_p+vdW simulated crystallographic parameters, and the elastic tensor, phonon, and linear optical properties. Overall, the computationally cheap GGA-PBE+U_d+U_p with vdW force may have successfully probed the physical properties of BWO.

Received 29th September 2023
Accepted 1st December 2023

DOI: 10.1039/d3ra06648g

rsc.li/rsc-advances

1 Introduction

Semiconductor oxides based on benign and stable bismuth (Bi) have reigned supreme in visible-light-induced photocatalytic applications to mitigate disconcerting environmental issues.[1–4] The Bi brings about many interesting properties owing to its stereochemical and lone-pair activity, sp coupling, and spin–orbit interaction.[5–8] Tungsten (W), with partially filled 5d states in its oxides, also holds promise for photocatalytic actions.[9–11] Their combined oxide bismuth tungstate Bi_2WO_6 (BWO) turned out to be an n-type semiconducting material belonging to the Aurivillius phase where pseudo-perovskite $[WO_4]^{2-}$ octahedral layers are stacked between $[Bi_2O_2]^{2+}$ layers and possesses a band gap of ~2.8 eV.[12,13] The BWO has manifested many fascinating photocatalytic, dielectric, ferroelectric, and piezoelectric properties that are pertinent to the photodegradation of pollutants, water splitting, and photovoltaic applications.[14]

Several experimental methods like solid-state reactions, and sol–gel, hydrothermal, solvothermal, and microwave-assisted techniques have been used to synthesize BWO.[14,15] The first principles simulations using density functional theory (DFT) can serve as an indispensable tool for understanding the functional properties of BWO.[16,17] The accuracy of DFT simulations suffers critically due to the improper modeling of partially filled W-5d orbitals in BWO for generalized gradient approximation (GGA) of Perdew–Burke–Ernzerhof (PBE).[18,19] The Hubbard interaction corrected GGA-PBE+U_d version, where the U_d is applied to the W-5d, was used to study polaron formation

[a]*Materials Science Research Laboratory, Department of Electrical and Electronic Engineering, University of Dhaka, Dhaka 1000, Bangladesh. E-mail: imtiaz@du.ac.bd*
[b]*Department of Materials Science and Engineering, Rensselaer Polytechnic Institute, Troy, NY, USA*
[c]*Semiconductor Technology Research Centre, University of Dhaka, Dhaka 1000, Bangladesh*
[d]*Institute of Mining, Mineralogy and Metallurgy, Bangladesh Council of Scientific and Industrial Research, Joypurhat 5900, Bangladesh*
[e]*Materials Science Division, Atomic Energy Centre, Dhaka 1000, Bangladesh*
[f]*Institute of Energy Research and Development, Bangladesh Council of Scientific and Industrial Research, Dhaka 1205, Bangladesh*
[g]*Institute of Glass and Ceramic Research and Testing, Bangladesh Council of Scientific and Industrial Research, Dhaka 1205, Bangladesh*
[h]*Institute of Food Science and Technology, Bangladesh Council of Scientific and Industrial Research, Dhaka 1205, Bangladesh*
[i]*Biomedical and Toxicological Research Institute, Bangladesh Council of Scientific and Industrial Research, Dhaka 1205, Bangladesh*
[j]*Nanophysics and Soft Matter Laboratory, Department of Physics, University of Dhaka, Dhaka 1000, Bangladesh*

† Electronic supplementary information (ESI) available. See DOI: https://doi.org/10.1039/d3ra06648g

effects, seems to underestimate the electronic band gap of bulk BWO measured from the density of states (DOS) compared to the experimental observations.[20] Moreover, the indirect nature of the BWO band gap is not confirmed by the electronic band structure (BS) simulation based on GGA-PBE+U_d.[21,22] The computationally intense and sophisticated Heyd–Scuseria–Ernzerhof (HSE06) functional with 25% Hartree–Fock (HF) exact-exchange mixing overestimates the band gap in electronic BS simulations.[23] In recent times, corrections to electronic and optical properties have been simulated using the quasi-particle GW method with spin–orbit interaction turned on.[24] The computational burden of these advanced many-body methods can be huge and requires careful parameter optimization to keep the simulation tractable. A computationally cheap DFT functional capable of reliably simulating the physical properties of BWO is often desired. To this aim, we invoke the GGA-PBE+U_d+U_p formalism including the van der Waals (vdW) force to model the observations regarding experimentally synthesized BWO.[25,26]

Here we synthesized BWO following solid-state reaction and hydrothermal techniques. The X-ray diffraction, Raman, and Fourier transform infrared spectroscopy were used to confirm the desired orthorhombic $Pca2_1$ phase purity in all synthesized samples. The surface morphology and chemical purity analysis were performed using field emission scanning electron micrographs and energy-dispersive X-ray spectroscopy, respectively. High-resolution Transmission Electron Microscopy and X-ray Photoelectron Spectroscopy were used to probe the crystallinity and chemical states of the samples. The diffuse reflectance measurements were performed to estimate the electronic band gaps of the BWO samples. The photocatalytic degradation performance of all BWO samples in degrading the methylene blue (MB) dye is studied with UV-vis absorption measurements. We tuned the Hubbard (U_d, U_p) corrections within the GGA-PBE+U_d+U_p formalism including the vdW force to reliably reproduce the electronic properties of the experimentally synthesized BWO samples. The optimized GGA-PBE+U_d+U_p+vdW simulated results were benchmarked against computationally intense HSE06 and PBE-HF20% functionals where the Hartree–Fock (HF) exact-exchange parameter α_{HF} is tuned. The elastic tensor, vibrational phonon, and linear optical properties were probed in detail to justify the use of the optimized (U_d, U_p) values.

2 Methodology

2.1 Computational details

The projector augmented wave (PAW) based spin-polarized DFT simulations were performed using the Vienna *Ab Initio* Simulation Package (VASP) code.[27,28] The orthorhombic Bi_2WO_6 unit cell contains a total of 36 atoms comprising of Bi (8), W (4), and O (24) atoms. The PAW considered Bi $5d^{10}6s^26p^3$ (15), W $5p^65d^46s^2$ (12), and O $2s^22p^4$ (6) electrons as valence and the remaining ones are treated as the core. The plane wave basis expansion is used with a 580 eV energy cutoff. A $9 \times 9 \times 3$ Monkhorst–Pack k-mesh was used to sample the Brillouin Zone (BZ) in structural relaxation (Hellmann–Feynman force convergence 10^{-4} eV Å^{-1}) and single point self-consistent total energy (convergence accuracy of 10^{-8} eV per atom) calculations. The Quantum-ESPRESSO (QE) code was used to calculate the Raman tensor using the finite difference method with similar values for the simulation parameters.

The exchange–correlation (xc) functional dictates the DFT simulation accuracy and complexity.[29,30] The finite difference technique was used to simulate the Raman tensor using GGA-PBE and GGA-PBE+U_d+U_p functionals.[28,31–37] The GGA-PBE functional leads to localized *d* orbital binding energy underestimation that inflates its hybridization with *p* orbitals.[16,17,38–40] This spurious p–d coupling enhancement shifts the valence band maximum (VBM) up in energy, leading to band gap narrowing effects.[41] Moreover, the W-5d orbitals in BWO are less spatially localized than many 3d orbitals present in transition metals.[42] The interaction and correlation corrections have been applied to W-5d and O-2p orbitals within the GGA-PBE+U_d+U_p approach.[25,26,43,44] The lattice parameter overestimation in GGA-PBE and GGA-PBE+U_d+U_p was reduced by incorporating the van der Waals (vdW) force with DFT-D3 method including Becke–Johnson (BJ) damping.[45] The phonon DOS, BS, and Born charge were simulated using the finite difference method in Phonopy based on $2 \times 2 \times 2$ supercell containing 288 atoms.[46,47] The 2nd order force constants are calculated for GGA-PBE and GGA-PBE+U_d+U_p with vdW taken into account. Moreover, HSE06 hybrid functional with the Hartree–Fock (HF) exact exchange mixing parameter $\alpha_{HF} = 25\%$ was used to simulate electronic and optical properties.[17,38,48–52] The α_{HF} is tuned to 20% as PBE-HF20% functional to obtain better agreement with GGA-PBE+U_d+U_p+vdW simulation and experimentally measured electronic band gap.[53–55] The PBE-HFα_{HF}% functional use HSE screened approach similar to HSE06 with xc energy E_{xc}^{HSE} given in terms of short-range (SR) and long-range (LR) terms as

$$E_{xc}^{HSE} = \alpha_{HF}E_x^{HF,SR}(\mu) + (1 - \alpha_{HF})E_x^{PBE,SR}(\mu) + E_x^{PBE,LR}(\mu) + E_c^{PBE}(\mu) \quad (1)$$

where the screening parameter μ in hybrid functionals was set to 0.2 Å^{-1}.[56] The WANNIER90 tool is used to keep the computational burden manageable in hybrid functional-based electronic BS simulations.[17,39,57,58] The optical properties are derived from complex dielectric constant simulations for GGA-PBE+vdW, GGA-PBE+U_d+U_p+vdW, HSE06 and PBE-HF20% functionals.[16,17,38,39]

2.2 Sample preparation

2.2.1 Solid-state reaction. Solid-state reaction-based sample was synthesized following our previous works in ref. 16, 17, 38, 59 and 60. The stoichiometric amount of $Bi(NO_3)_3 \cdot 5H_2O$ (Merck Germany, 99+% pure) and $Na_2WO_4 \cdot 2H_2O$ (Merck Germany, 99+% pure) were weighed as precursor materials. The $Bi(NO_3)_3 \cdot 5H_2O$ was hand milled for 30 min using an agate mortar. Next $Na_2WO_4 \cdot 2H_2O$ was added to it and the mixture was hand milled again for 2 h. Circular pellets made in a hydraulic press (Weber-Pressen) with 25 kN uni-axial force were sintered at 300 °C for 2 h. The pre-sintered pellets were crushed into fine powder form before being

subjected to subsequent sintering at higher temperatures. After a number of trial sintering, the optimum temperature for phase pure BWO was found to be 650 °C, and termed as SBWO hereafter.

2.2.2 Hydrothermal synthesis. The 20 mmol (9.9 g) $Bi(NO_3)_3 \cdot 5H_2O$ (Merck Germany, 99+% pure) and 10 mmol (3.332 g) $Na_2WO_4 \cdot 2H_2O$ were first dissolved homogeneously by vigorous stirring and sonication in 9 mL of 20% HNO_3 solution separately. A mixture was formed after 80 mL of ethylene glycol was poured into this solution. The pH of the mixture was set to 7.5 by adding a required portion of KOH and converted to a suspension by subsequent magnetic stirring for 1 h. The resulting suspension was loaded into a 100 mL Teflon-lined autoclave and then reacted at 180 °C for 20 h inside an oven. Subsequently, the reactor was cooled to room temperature naturally. The resulting product was centrifuged at 10000 rpm for 10 min with first ethanol and then distilled water for 6 consecutive cycles and then heated at 80 °C for 16 h to obtain powder form samples termed as HBWO-U. This unsintered HBWO-U sample was sintered at 400 °C for 2 h and the resulting sample was labeled as HBWO-S subsequently.

2.2.3 Photocatalytic sample preparation. The 100 mL of MB solution was prepared at 10 ppm concentration. For each of the SBWO, HBWO-U, and HBWO-S photocatalysts, 1 g L^{-1} solutions were prepared at pH = 10 with the proper amount of NH_4OH in the dye-photocatalyst mixture. The adsorption–desorption equilibrium was attained to form suspension by constant magnetic stirring for 30 min in the dark. The liquid suspensions were under constant magnetic stirring during the optical exposure from the Hg–Xe lamp. The stirring avoids inhomogeneity of the MB concentration across the solution and prevents spurious degradation effects. High-speed centrifuging (12 000 rpm, 5 cycles) facilitated the photocatalyst removal from the dye solution. The UV-vis absorption measurements are taken in finite intervals for SBWO (30 min), HBWO-U (10 min), and HBWO-S (10 min) to evaluate the photocatalytic degradation performances.

2.3 Characterization techniques

Programmable high-temperature Muffle Furnaces (Nabertherm LT 5/14 & Kejia M1700) were used for sample sintering. The powdered X-ray Diffraction (XRD) data within 10° to 80° diffraction angle were recorded at 35 kV tube voltage and 20 mA tube current with Cu K_α radiation (λ = 0.15418 nm) in a Rigaku SmartLab SE multipurpose XRD system. The Raman bands for the samples are obtained from 532 nm laser excitation in a Horiba Scientific Confocal Raman Microscope LabRAM HR Evolution. The PerkinElmer Spectrum Fourier Transform Infrared (FTIR) spectrometer was used to obtain the relevant IR absorption bands of the samples. The morphology and chemical purity of the SBWO sample were studied using a Scanning Electron Microscope (SEM, AVO Research) and Energy Dispersive X-ray Spectroscopy (EDX, EDAX Team) respectively. For hydrothermally synthesized samples, morphology studies were performed using Field Emission Scanning Electron Microscopy (FESEM, JEOL 7610F), Transmission Electron Microscopy (TEM), High-Resolution Transmission Electron Microscopy (HRTEM), and Selected Area Electron Diffraction (SAED) measurements using Thermo Fischer Scientific Talos F200X. The K_α X-ray Photoelectron Spectroscopy (XPS) was done using Thermo Fischer Scientific X-ray Photoelectron Spectrometer where the 284.8 eV binding energy C-1s level was used for calibration. The optical characterizations were performed by UV-vis diffuse reflectance measurements in a Shimadzu UV-2600i UV-Vis-NIR spectrometer. The samples' photocatalytic performance was estimated from UV-vis absorption spectra measured with a Shimadzu UV-1900i spectrometer.

3 Results and discussion

3.1 X-Ray diffraction analysis

The powder XRD data of solid-state reaction synthesis-based samples with different sintering temperatures of 400, 500, 600, 650, and 800 °C are presented in Fig. 1(a). The phase pure Bi_2WO_6 was evident in the SBWO sample sintered at 650 °C. In samples with other sintering temperatures, the Bi_2O_3 impurity peaks were present. The Rietveld refinement in Fig. 1(b) revealed a pure orthorhombic phase in SBWO with the goodness of fitting χ^2 = 1.75. The orthorhombic phase was also confirmed both in HBWO-U (χ^2 = 1.45) and HBWO-S (χ^2 = 1.27) samples as presented in Fig. 1(c) and (d), respectively. The orthorhombic phase belongs to the $Pca2_1$ space group and point group *mm*2 (JCPDS No. 39-0256). No unwanted impurity peaks were detected. The sharp intense peaks corroborate good crystallinity in all samples. The diffraction peak intensity of HBWO-U is decreased and increased compared to SBWO and HBWO-S samples, respectively. This is suggestive of crystallite growth with temperature. The broadening in the (131) peak for hydrothermally synthesized HBWO-U and HBWO-S as compared to that of the SBWO sample indicates the existence of small-size particles in them. The line width analysis with the Scherrer formula revealed average crystallite sizes to be 22 nm (SBWO), 8 nm (HBWO-U), and 12 nm (HBWO-S). The most intense diffraction peak in all samples is (1 3 1) which is in line with (1 2*m* + 1 1) peak of Aurivillius phases.[61]

Table S1† reveals that both GGA-PBE and GGA-PBE+U_d+U_p functionals overestimated the unit cell volume by ~7.7% and ~5.93% compared to the experimental observations. The inclusion of vdW force provides correction to the lattice parameters and reduces the unit cell volume estimation error to 3.79% and 2.18% for GGA-PBE+vdW and GGA-PBE+U_d+U_p+-vdW, respectively, see Table S2.† Hence the inclusion of vdW force has the potential to improve the reliability of the DFT simulations.

3.2 Raman analysis

The measured Raman spectra of the samples are presented in Fig. 2. The group theory dictates A_{1g}, B_{1g} and E_g symmetry modes to be Raman active near the BZ center of orthorhombic Bi_2WO_6.[62–64] All experimentally observed Raman bands are interpreted in accordance with the corresponding atomic

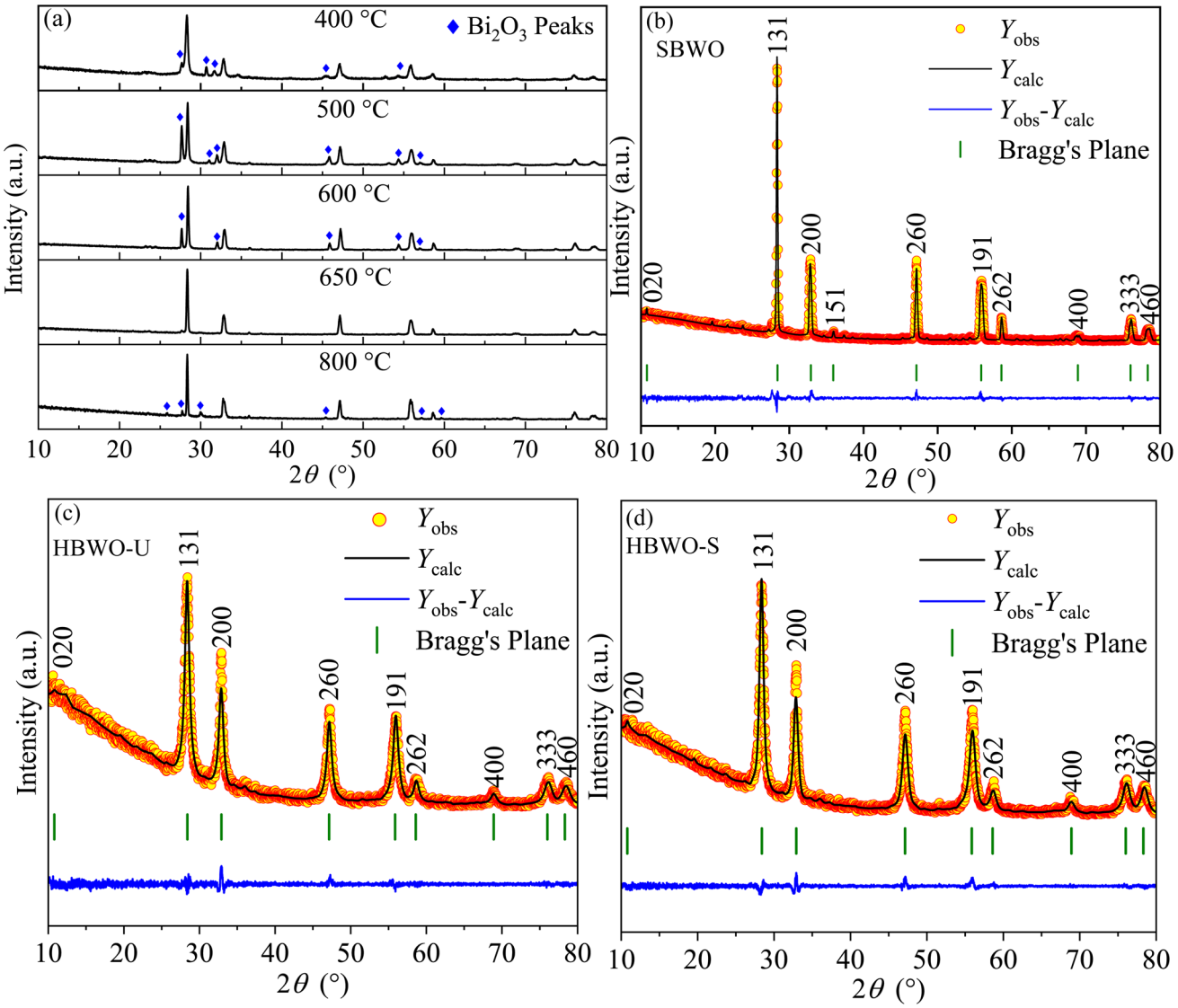

Fig. 1 (a) Powder XRD patterns of BWO samples with different sintering temperatures prepared in solid-state reaction. Rietveld refined XRD patterns on top of (b) experimentally observed data of SBWO, hydrothermally synthesized (c) unsintered HBWO-U, and (d) sintered HBWO-S samples. The yellow circles are the experimental data points (Y_{obs}), the black solid line represents the calculated refined pattern Y_{cal}, the bottom blue curve Y_{diff} shows the difference between the Y_{obs} and Y_{cal} values.

motion along with the DFT simulated peaks in Table S3†.[65] The phase-independent external lattice modes are located near 130 (E_g) and 150 cm^{-1} (A_{1g}). The antisymmetric deformation (B_{1g}) of WO_6 octahedra stems Raman bands near ~220 nm in HBWO-U and HBWO-S samples. The Raman peaks near ~250 cm^{-1} can be explicated as symmetric bending vibration (A_{1g}) of Bi–O bonds. The bands around ~280 and ~410 cm^{-1} arose from antisymmetric bending vibrations (E_g) of WO_6 octahedra. The coupled Bi^{3+} and WO_6^{6-} unit undergoes simultaneous translation (E_g) which produce Raman bands near 300 cm^{-1}. The asymmetric bridge mode (B_{1g}) of the WO_6 chain bridge originates the Raman bands at ~710 and ~800 cm^{-1}. The peaks near 724 and ~814 cm^{-1} can be interpreted as asymmetric stretching modes (B_{1g}) of O–W–O bonds in the WO_6 octahedral cluster. Both GGA-PBE and GGA-PBE+U_p+U_d derived Raman peaks are in good agreement with the experimental observations.

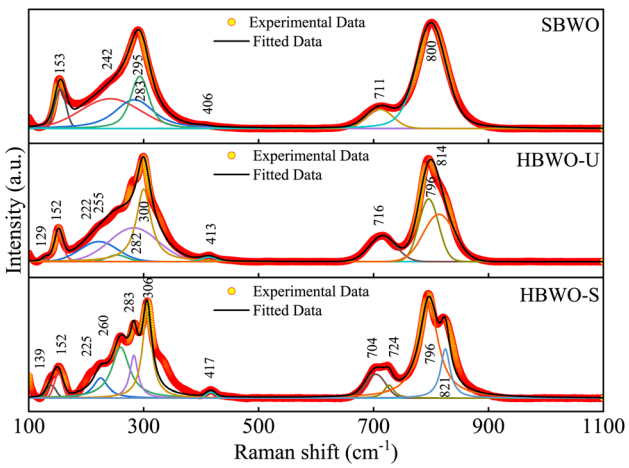

Fig. 2 Deconvoluted room temperature Raman spectra of SBWO, HBWO-U, and HBWO-S.

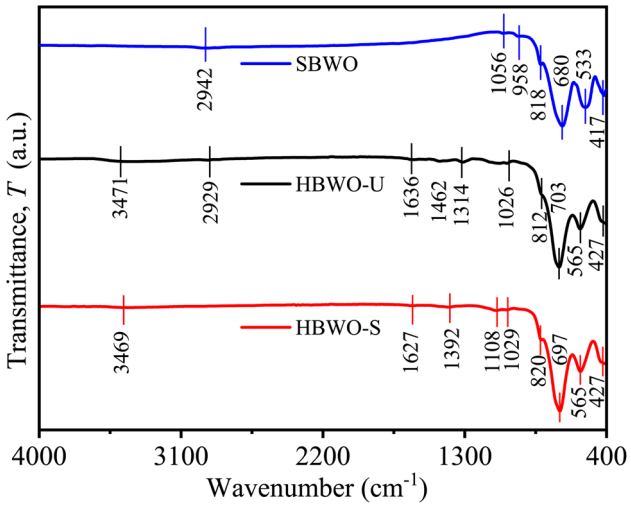

Fig. 3 FTIR spectra of SBWO, HBWO-U, and HBWO-S.

3.3 Fourier transform infrared spectroscopy

The FTIR spectra of SBWO, HBWO-U, and HBWO-S samples are displayed in Fig. 3. The observed FTIR absorption bands are assigned to their respective atomic bond vibrations in Table S4.†[66,67] The symmetric Bi–O stretching stems the IR absorption near ~427 and ~820 cm^{-1}. The absorption originating from antisymmetric Bi–O–Bi stretching can be seen in 533 and 565 cm^{-1}. The IR bands (~680, ~700) and (~1056, ~1029) cm^{-1} can be assigned to W–O symmetric stretching. The 958 cm^{-1} (SBWO) and ~3471 (HBWO-U, and HBWO-S) cm^{-1} IR absorption can be ascribed to the bending vibration of O–H bonds in water molecules present in the sample. For hydrothermally synthesized samples, the O-H stretching vibration is located near ~1634 cm^{-1}. The symmetric stretching of C=O bonds appear near 1314 cm^{-1} (HBWO-U) and 1392 cm^{-1} (HBWO-S). The adsorption of atmospheric CO_2 may have originated these IR bands.

3.4 Morphology analysis

Fig. 4 presents the SEM and FESEM micrographs. The SBWO grains in Fig. 4(a) were irregularly shaped with an average size of ~175 nm. The higher sintering temperature of the solid-state reaction may have provided enough energy for this irregular thermal grain nucleation and growth. For the HBWO-U sample, a mixture of rectangular and spherically shaped particles with 55 nm size are visible in the FESEM micrograph presented in

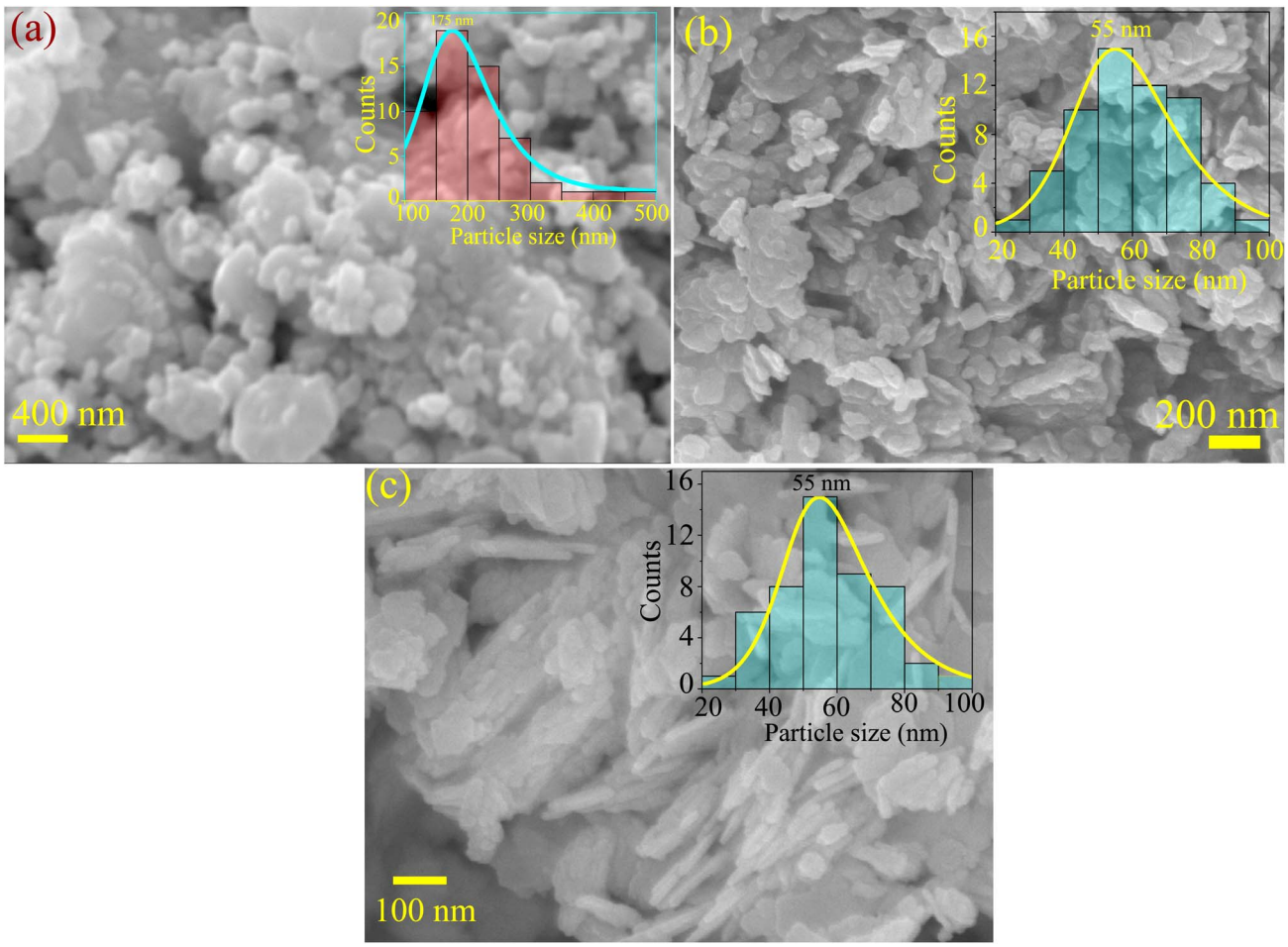

Fig. 4 (a) SEM micrograph of SBWO. FESEM micrographs of (b) HBWO-U, and (c) HBWO-S.

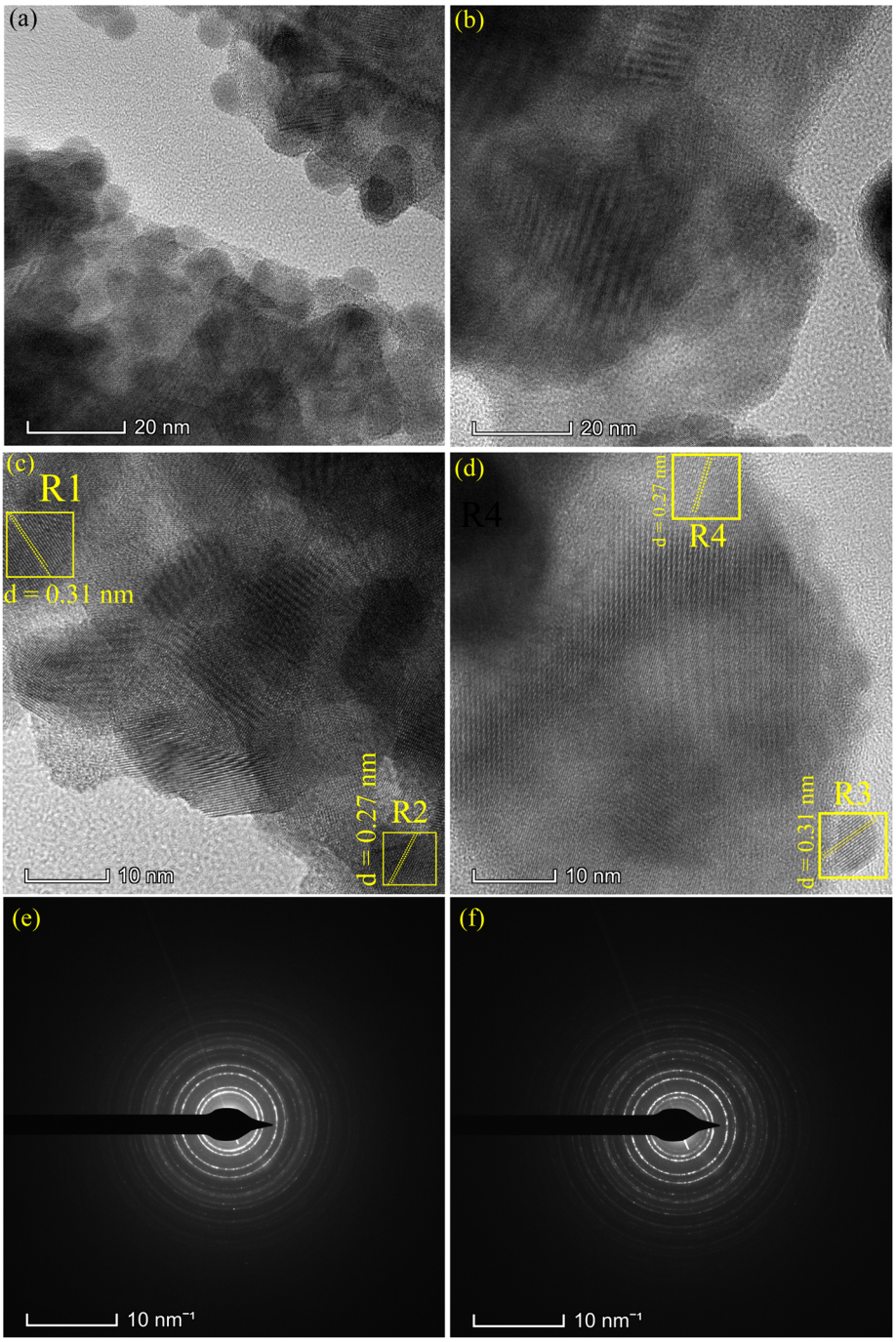

Fig. 5 TEM images of (a) HBWO-U, (b) HBWO-S. HRTEM images of (c) HBWO-U, and (d) HBWO-S. SAED images of (e) HBWO-U, and (f) HBWO-S.

Fig. 4(b). The subsequent sintering promoted rectangular rod-like features in particles as presented in Fig. 4(c). The EDX spectra of Bi, W, and O in Fig. S1† are also in good agreement with that of Bi_2WO_6.[68–70] The experimental atomic percentage (at%) and weight percentage (wt%) of Bi, W, and O in Table S5† conform to that of theoretical values conforming to the atomic ratio of Bi_2WO_6. Fig. 5 presents the HRTEM, and SAED measurements of HBWO-U and HBWO-S samples. Fig. 5(a) shows randomly distributed spherical-shaped particles with a diameter of ~10 nm in HBWO-U sample. In the case of HBWO-S, uniform sheets are revealed in Fig. 5(b). HRTEM images in Fig. 5(c) and (d) show distinct lattice fringes separated by 0.31 (R1 & R3) and 0.27 (R2 & R4) nm that correspond to *d*-spacing of (131) and (020) crystallographic planes of Bi_2WO_6.[70–72] The non-uniform intensity of concentric circular-shaped diffraction rings visible in SAED images in Fig. 5(e) and (f) are characteristic of the textured polycrystalline nature of the samples.

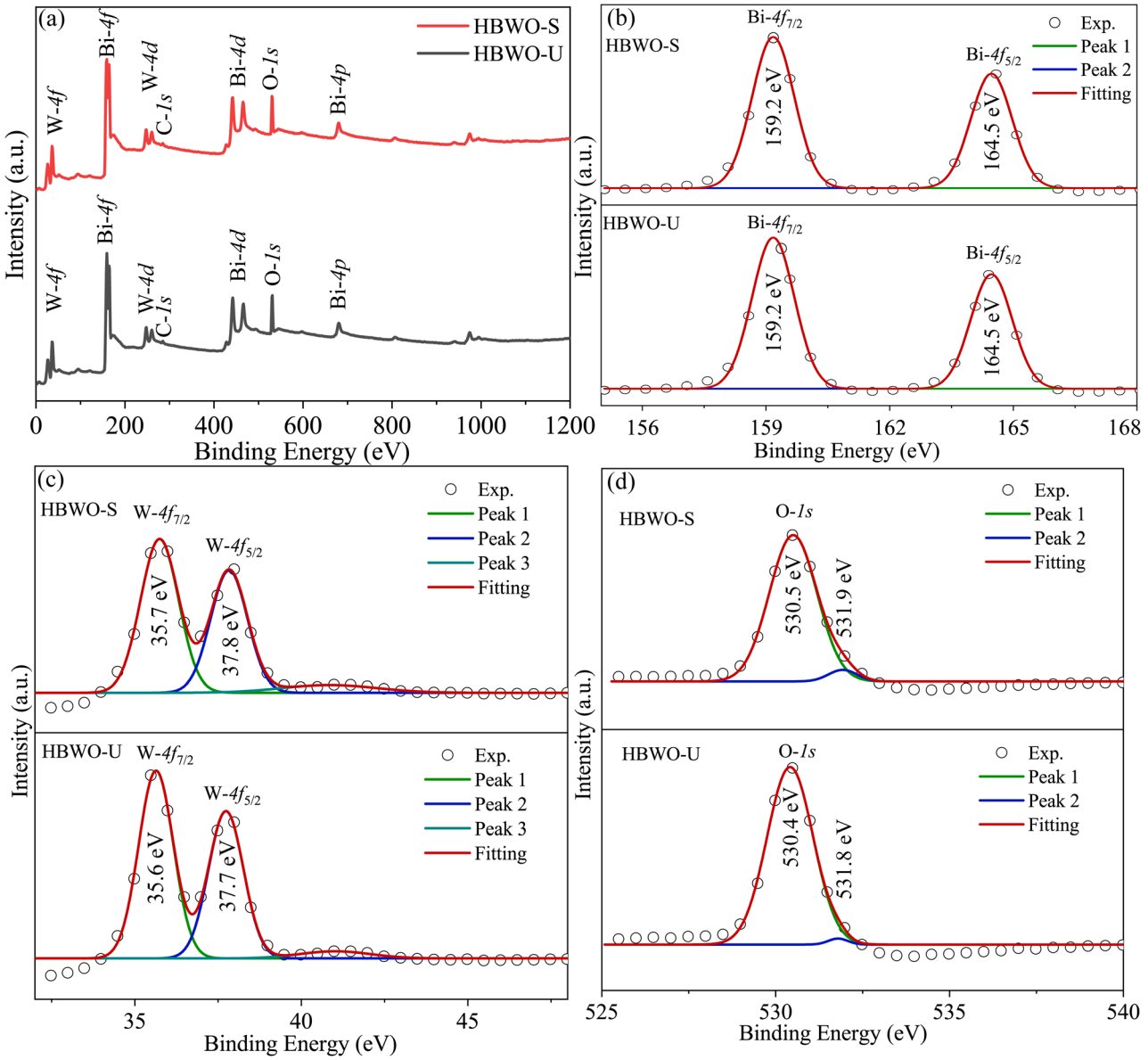

Fig. 6 (a) XPS full survey, and core level XPS spectra of (b) Bi-4f, (c) W-4f, and (d) O-1s for HBWO-U and HBWO-S.

3.5 X-ray Photoelectron Spectroscopy

The full XPS spectrum in Fig. 6(a) revealed Bi, W, and O elements in HBWO-U and HBWO-S samples.[73] The XPS peaks at 159.2 and 164.5 eV in Fig. 6(b) are characteristic to Bi-4$f_{7/2}$ and Bi-4$f_{5/2}$ spin–orbit splitting of Bi^{3+} in BWO.[67] The W-4$f_{7/2}$ and W-4$f_{5/2}$ XPS peaks at 35.6 and 37.7 eV of HBWO-U are slightly shifted to higher binding energies of 35.7 and 37.8 eV for HBWO-S as shown in Fig. 6(c), and are ascribed to W^{6+} in BWO lattice.[74,75] The O-1s peak at 530.4 eV (530.5 eV) of HBWO-U (HBWO-S) in Fig. 6(d) can be designated to lattice oxygen of W–O and Bi–O bonding. The weak XPS peak at 531.8 eV (531.9 eV) of HBWO-U (HBWO-S) can be attributed to C=O bonds adsorbed on the surface of samples.[72]

3.6 UV-vis spectroscopy

The Kubelka–Munk function $F(R_\infty)$ was used to convert the UV-vis diffuse reflectance into absorption as presented in Fig. 7(a). The samples' steep absorption edges lie within the 350-450 nm wavelength bands. The band gap E_g was estimated from

$$[F(R_\infty)h\nu]^{1/\gamma} = A(h\nu - E_g), \quad (2)$$

where A, h, and ν represent proportionality constant, Planck's constant, and incident photon frequency, respectively. The parameter γ sets the direct and indirect nature of the band gap. By extrapolating the Tauc's plots onto the energy axes for $\gamma = 2$ in Fig. 7(b), the indirect E_g turned out to be 2.84, 3.13, and

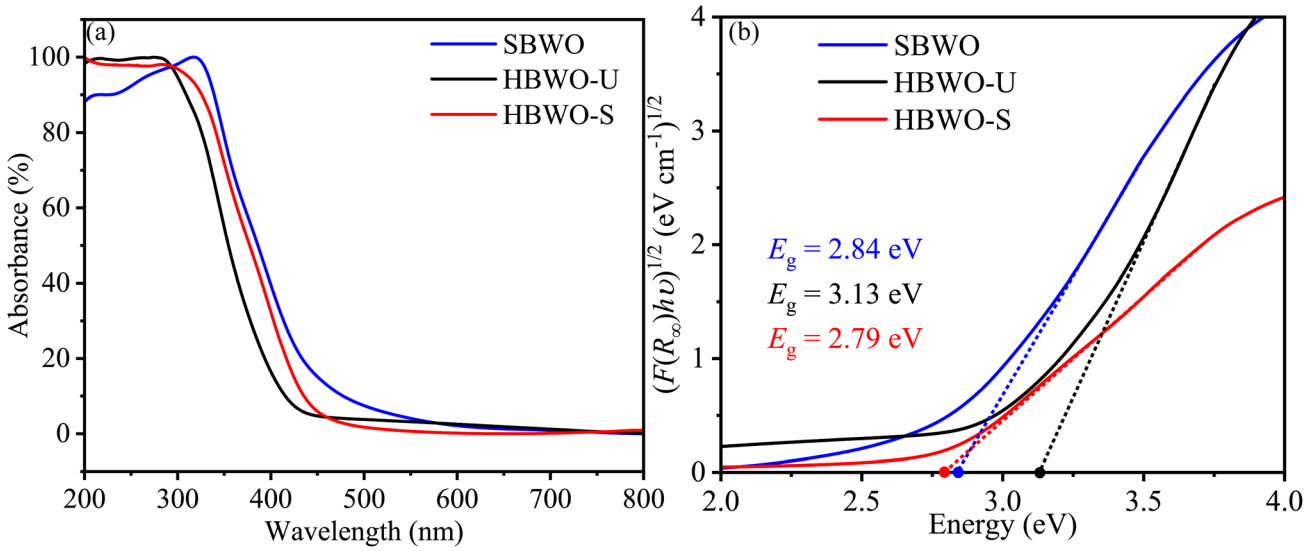

Fig. 7 (a) UV-vis diffuse absorption spectra, and (b) Tauc plots of SBWO, HBWO-U and HBWO-S samples.

2.79 eV for SBWO, HBWO-U, and HBWO-S, respectively. The measured band gaps are consistent with that of the ref. 75–79.

3.7 Photocatalytic measurements

The MB photocatalytic degradation of SBWO, HBWO-U, and HBWO-S are estimated from UV-vis absorption measurements as displayed in Fig. 8. The photocatalyst and MB dye concentrations are set to 1 g L^{-1} and 10 ppm, respectively at pH = 10 in all cases. The reduction of MB characteristic intensity peak at 663 nm over exposure time indicates complete annihilation of it in cases of SBWO (180 min) and HBWO-U (60 min). To illustrate the significant degradation of HBWO-U in the dark, absorption spectra were recorded for one sample placed in the darkness and another under illumination, see Fig. 9(a) and (b). The absorption spectra are identical for the initial 30 min dark condition as expected. Because of the MB adsorption onto the photocatalyst, MB degradation in Fig. 9(a) continues as time progresses in the dark condition. The MB degradation Fig. 9(b) is much faster due to the optical exposure case. The absorption curve nearly flattens and loses its distinctive shape just after 30 min of illumination. The overall photocatalytic efficiencies are estimated by plotting C/C_0 *vs.* irradiation time in Fig. 10(a), where C_0 and C stand for the MB concentration at initial and some specific time, respectively. The HBWO-S degraded 60% of

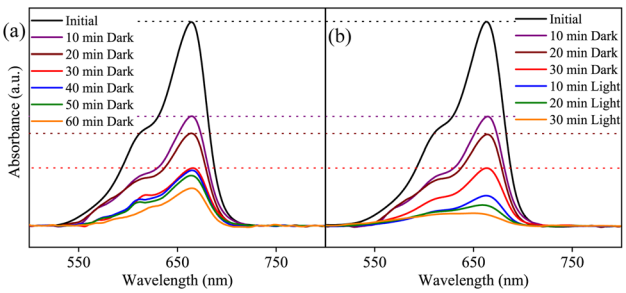

Fig. 9 The photocatalytic degradation measurements from UV-vis absorption spectra of SBWO-U (a) in dark, and (b) under optical exposure.

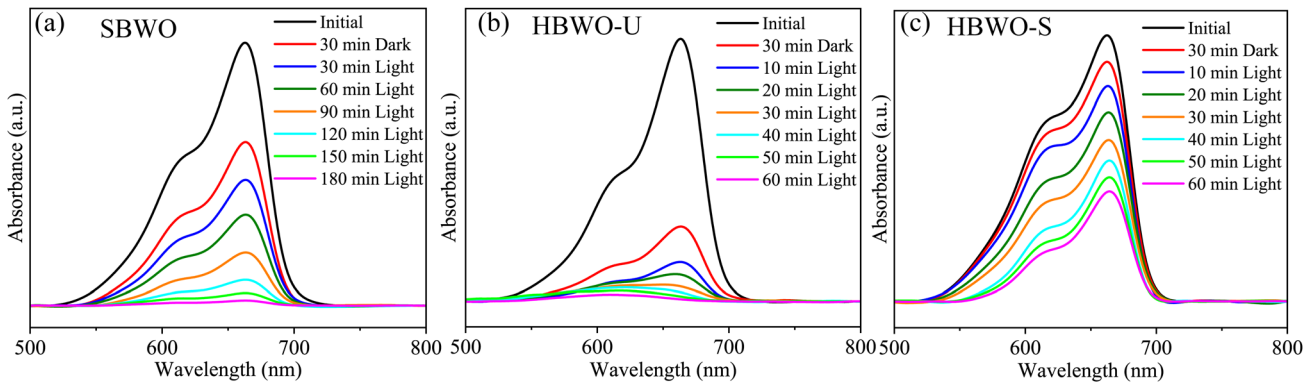

Fig. 8 The photocatalytic degradation measurements from UV-vis absorption spectra of (a) SBWO, (b) HBWO-U, and (c) HBWO-S photocatalysts (1 g L^{-1}) with 10 ppm MB dye.

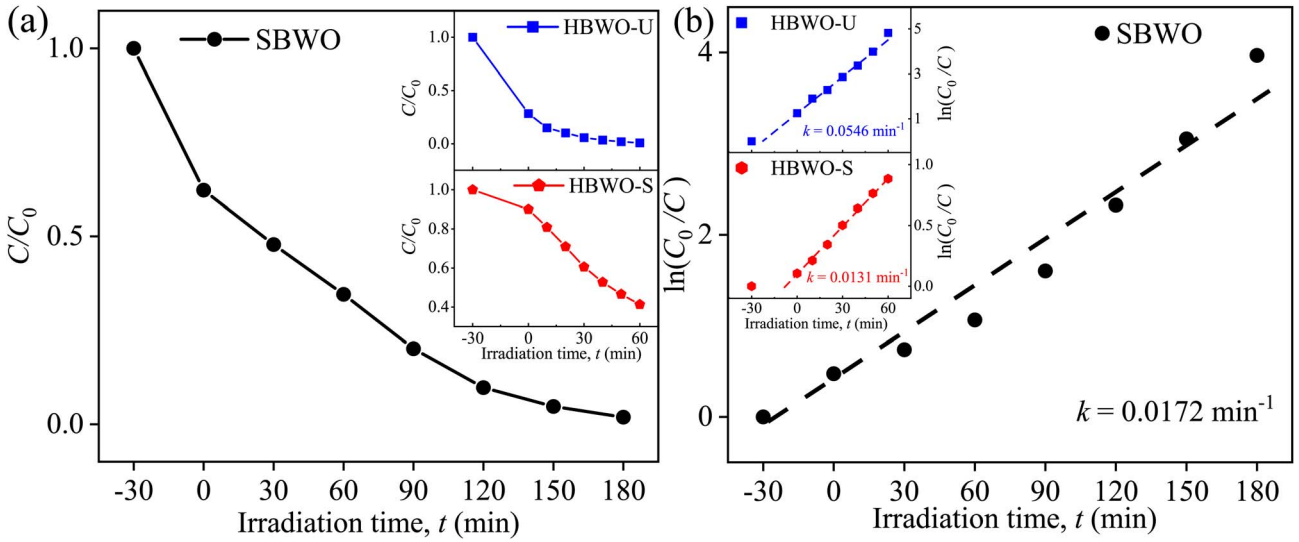

Fig. 10 (a) Time-dependent photocatalytic degradation fraction C/C_0, (b) linear fitted time-dependent photocatalytic degradation fraction of 10 ppm MB for 1 g L^{-1} SBWO, HBWO-U, and HBWO-S photocatalysts at pH = 10.

MB in 60 min of irradiation as presented in Fig. 10(a) (inset). The pseudo-first-order degradation kinetics is captured in Fig. 10(b) with Langmuir–Hinshelwood model using $\ln(C_0/C) = kt$. By linear fitting the data, the reaction rate k is estimated to be 0.0172 (SBWO), 0.0546 (HBWO-U), and 0.0131 min^{-1} (HBWO-S). The observed binding energy increment for W and O species as shown in Section 3.5 may have degraded the photocatalytic activity of HBWO-S compared to the HBWO-U sample.

3.8 Electronic properties simulation

The band gap E_g is measured from the total density of states (TDOS) and its projections onto different relevant orbitals (PDOS), see Fig. S2–S7.† It is evident in Fig. 11(a) that beyond $U_d = U_p = 9$ eV, the vdW force have negligible effect on E_g. Fig. 11(b) reveals E_g of ~2.61 eV, closer to experimental E_g of SBWO (2.84 eV) and HBWO-S (2.79 eV), for $U_d = U_p = 14$ eV with vdW force in effect. Moreover, the HSE06 ($\alpha_{HF} = 25\%$) provides an overestimation of E_g (2.98 eV) in Fig. 11(c). By tuning the α_{HF} to 20% in HSE screened approach, the PBE-HF20% functional yields $E_g = 2.79$ eV. For all functionals, the DOS share following common features: (i) the valence band (VB) stems from Bi-6s, Bi-6p, W-5p, W-5d, and O-2p orbitals, (ii) the top of the VB is comprised of hybridization among dominant O-2p and small Bi-6s and Bi-6p orbitals, (iii) the conduction band (CB) is formed with Bi6p, W-5d, O-2p and small portion of O-2s orbitals, and (iv) the bottom of the CB is mainly comprised of W-5d and O-2p orbital mixing.

The direct/indirect nature of the band gap can only be found from electronic BS simulation. The GGA-PBE in Fig. 12(a) provides an erroneous direct band gap for BWO even with the presence of vdW force. The valence band maxima (VBM) and conduction band minima (CBm) are located at the Γ point in BZ. But the optimum GA-PBE+U_d+U_p with the vdW force gives rise to the correct indirect transition as shown in Fig. 12(b). The VBM is located in $\Gamma \rightarrow X$ and the CBm occurred at Γ. The BS derived from HSE06 corroborated similar BS dispersion in Fig. 12(c) but overestimated the E_g (3.26 eV). With $\alpha_{HF} = 20\%$, the PBE-HF20% reduces the overestimation to 3.05 eV in Fig. 12(d). All these results corroborate the reliability of the GGA PBE+U_d+U_p+vdW simulations.

3.9 Optical properties simulation

The optical properties are defined by angular frequency ω dependent complex dielectric constant $\varepsilon(\omega) = \varepsilon_{real}(\omega) + i\varepsilon_{imag}(\omega)$. The ε_{imag} is derived from the dipole transition matrix and the Kramer–Kronig relation is used to obtain ε_{real} from it for different functionals. Fig. 13(a) provides evidence for close agreement of GGA-PBE+U_d+U_p+vdW with PBE-HF20% for ε_{real}. The perfect match in the $\omega \rightarrow 0$ limit corroborates the refractive indices agreement of both functionals. In Fig. 13(b), the steep rising edges of ε_{imag} along with the position of the peak in energy for both functionals are also in accord. The energy threshold beyond which optical absorption α shoots up depends on the band gap and varies for different functionals as shown in Fig. 13(c). The good agreement between the onset of absorption for GGA-PBE+U_d+U_p+vdW with PBE-HF20% is a direct consequence of their agreement in band gap estimation.

3.10 Elastic properties simulation

The structural stability of orthorhombic BWO was verified from elastic tensor C_{ij}s simulations for GGA-PBE, GGA-PBE+vdW, GGA-PBE+U_d+U_p, and GGA-PBE+U_d+U_p+vdW.[80,81] The simulated elastic properties are presented in Table S6.† The orthorhombic $Pca2_1$ symmetry defines nine independent C_{ij}s: C_{11}, C_{12}, C_{13}, C_{22}, C_{23}, C_{33}, C_{44}, C_{55}, and C_{66} that satisfy the required Born stability criterion

$$C_{11} > 0,\ C_{44} > 0,\ C_{55} > 0,\ C_{66} > 0,\ C_{11}C_{22} > C_{12}^2,\ C_{11}C_{22}C_{33} + 2C_{12}C_{13}C_{23} - C_{11}C_{23}^2 - C_{22}C_{13}^2 - C_{33}C_{12}^2 > 0, \quad (3)$$

regardless of the vdW force as can be seen from Table S5†.[82–84] The salient elastic properties like bulk-modulus (B_V, B_R and B_H),

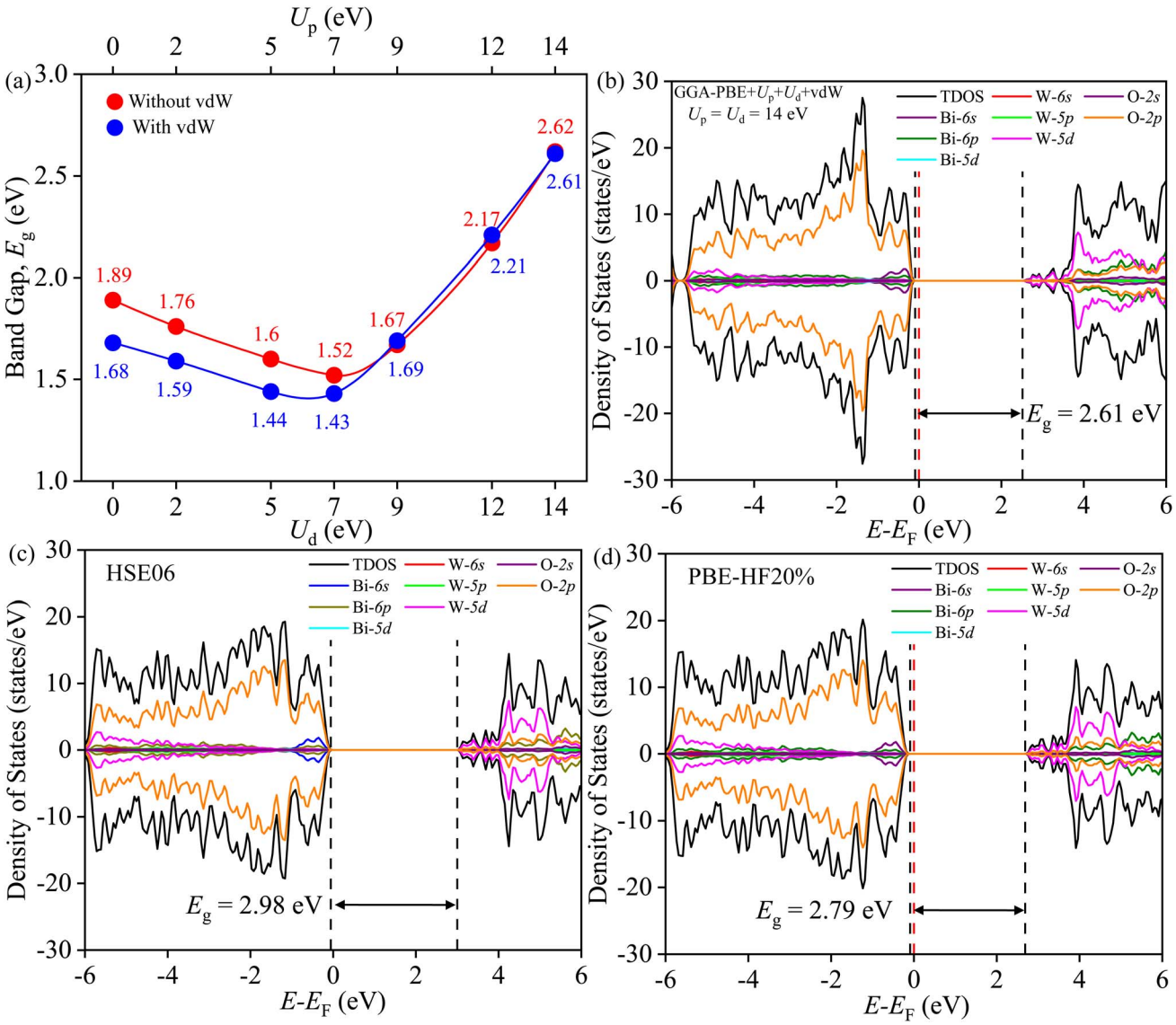

Fig. 11 (a) Band gap E_g tuning with U_d and U_p with and without vdW force, (b) TDOS and PDOS of BWO for GGA-PBE+U_d+U_p+vdW, (c) HSE06, and (d) PBE-HF20%.

shear modulus (G_V, G_R and G_H), Young's modulus (E_V, E_R and E_H), Poisson's ratio (ν_V, ν_R and ν_H) and Pugh's ratio (k_V, k_R and k_H) were simulated for Voigt (V), Reuss (R) and Hill (H) framework.[85–87] The Hubbard (U_d, U_p) corrections and the vdW force inflate the bulk, shear, and Young's moduli compared to that of GGA-PBE which imply plastic deformation and stiffness enhancement. The brittle nature of BWO is prevalent in all cases as Poisson's ratio stayed below the threshold value of 0.33. The Pugh's ratio is well below the brittle/ductile value of 1.75 which further confirms the brittle nature of BWO.

3.11 Phonon properties simulations

The dynamical stability can be probed from phonon modes of the material.[16,17,39,40] The simulated phonon BS and DOS using finite difference supercell method are shown in Fig. 14. The absence of imaginary frequency modes in the entire BZ corroborates the dynamical stability of HBWO for both GGA-PBE and GGA-PBE+U_d+U_p with vdW force in action. The supercell allows displacement distortion that helps to establish the dynamical stability of the BWO structure.[46,88,89] The Bi, W, and O have decreasing inertial resistance to atomic vibration due to a reduction in the atomic masses. The vibrational spectra of Bi (heavy), and O (light) dominate over 15–200 and 250–500 cm^{-1} ranges, respectively as shown in the phonon DOS of Fig. 14(a) and (b). The phonon DOS peaks are in good agreement with experimental FTIR peaks in Table S4.† The average of the diagonal Born effective charge (BEC) tensor elements in Table S7† yields +4.675, +7.66, and −2.97 for Bi, W, and O1 atoms. For $U_d = U_p = 14$ eV with vdW force, the born charge anomalies are increased due to electronic charge delocalization in favor of covalent bonding.

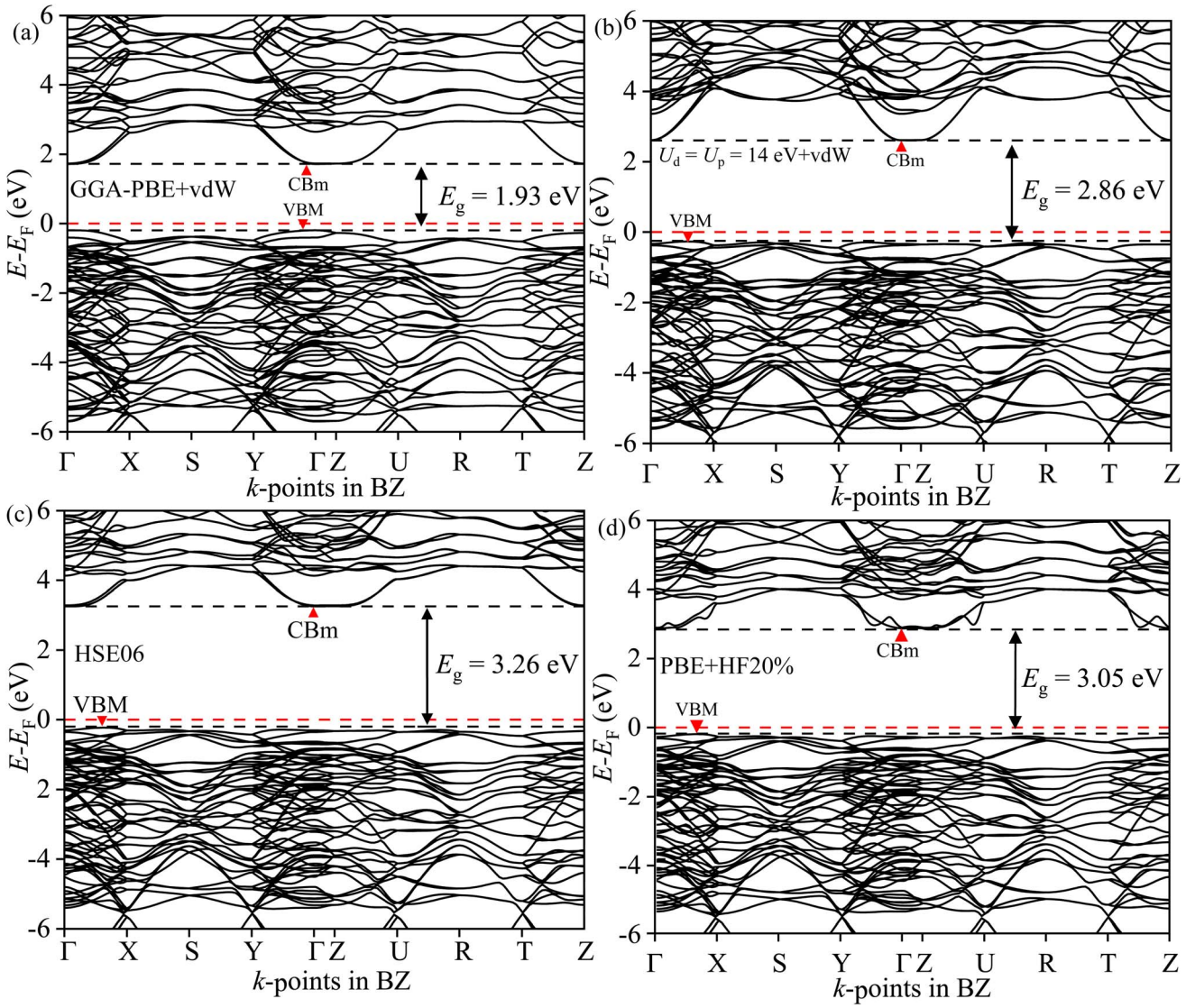

Fig. 12 Electronic BS of BWO along Γ, R, S, T, U, X, Y, and Z high symmetry k-points in BZ for (a) GGA-PBE+vdW, (b) GGA-PBE+U_d+U_p+vdW, (c) HSE06 and (d) PBE-HF20%.

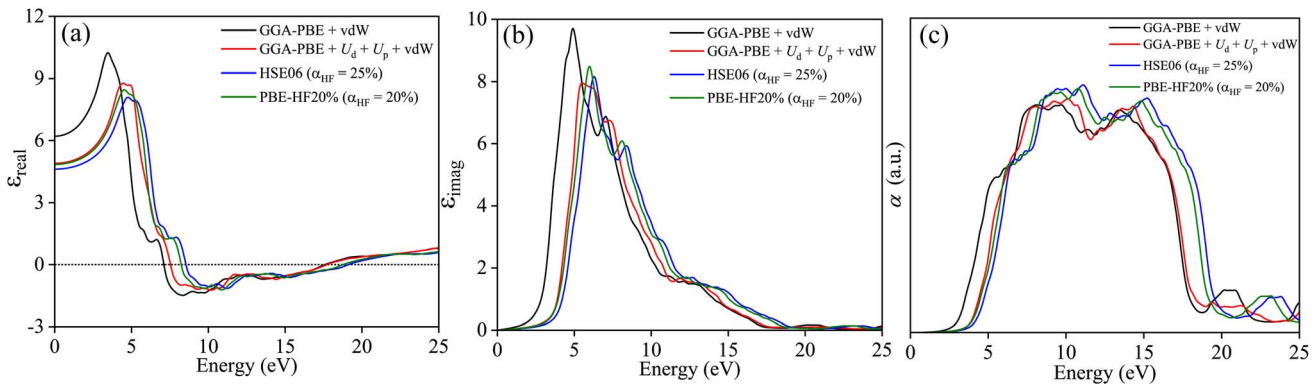

Fig. 13 (a) Real part of dielectric constant ε_{real}, (b) imaginary part of the dielectric constant ε_{imag}, and (c) absorption coefficient α as a function photon energy E calculated with GGA-PBE+vdW, GGA-PBE+U_p+U_d+vdW, HSE06 (α_{HF} = 25%), and PBE-HF20% (α_{HF} = 20%) averaged over three different polarization E_x, E_y and E_z.

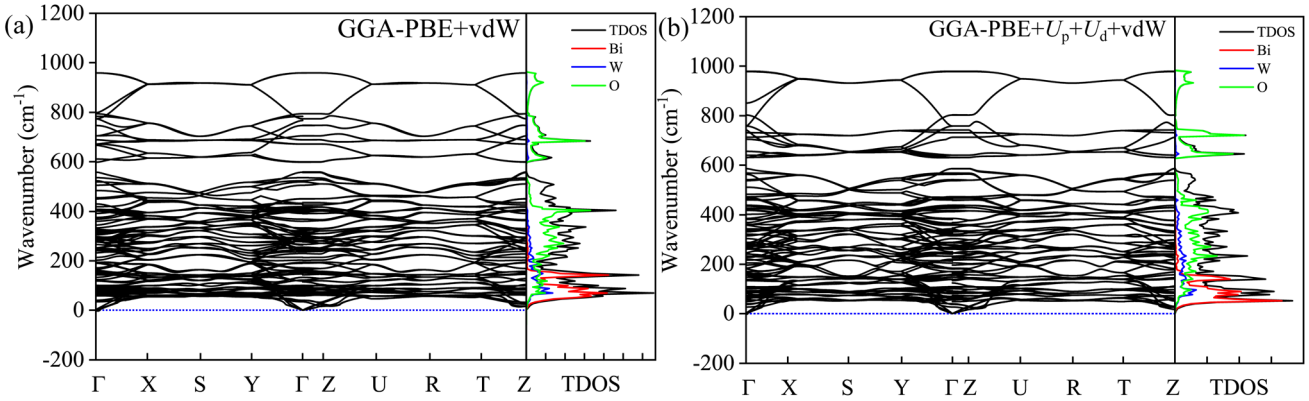

Fig. 14 Phonon BS, total DOS, and partial DOS of B, W, and O atoms in BWO using the finite-difference supercell approach for (a) GGA-PBE+vdW, and (b) GGA-PBE+U_d+U_p+vdW. The phonon BS is simulated along *Γ*, *R*, *S*, *T*, *U*, *X*, *Y*, and *Z* high symmetry *k*-points in BZ.

4 Conclusion

The orthorhombic $Pca2_1$ phase purity in the SBWO, HBWO-U, and HBWO-S samples was confirmed from XRD, Raman, and FTIR measurements. The morphology analysis revealed particle shapes to vary over rectangular, spherical, and rod-like features as per the FESEM measurements. The HRTEM images revealed randomly distributed particles with size ~10 nm in HBWO-U sample. The polycrystalline nature of samples is confirmed by ring-shaped SAED patterns. The UV-vis diffuse reflectance revealed indirect electronic band gap variation within the 2.79–3.23 eV energy window. The diluted Coulomb interaction of localized W-5d orbital is successfully modeled with computationally cheap GGA-PBE+U_d+U_p functional with the vdW force that reproduced experimentally observed crystallographic parameters, and electronic band gaps of as-synthesized samples. The use of optimized values of U_d and U_p is justified by reproducing the BWO electronic properties by tuning the Hartree–Fock exact-exchange mixing parameter α_{HF} from 25% in the HSE06 to 20% in PBE-HF20% functional. Moreover, the tuned GGA-PBE+U_d+U_p+vdW successfully probed the elastic tensor, phonon, and optical properties of BWO. Overall, the computationally cheap PBE+U_d+U_p with vdW force may have successfully modeled the relevant physical properties of BWO.

Data availability

The data that support the findings of this study are available from the corresponding author upon reasonable request.

Author contributions

I. A. planned and supervised the entire project, and wrote the original article. Q. S. H. synthesized the samples by hydrothermal methods and performed all photocatalytic measurements. M. S. synthesized samples with solid-state reaction technique. Q. S. H., S.·S.·N., S. A., and I. A. performed the DFT simulations. M. N. I. K. and H. N. helped with XRD, FTIR, TEM, HRTEM, and SAED measurements. M. S. B. provided the SEM and EDX measurements. U. S. A. performed the XPS measurements. S. J. helped with the Raman measurements. F. C. performed the FESEM measurements. K. S. H. helped with optical measurements. Q. S. H., S. M. S. I., T. A. M., and I. A. performed the data analysis.

Conflicts of interest

The authors declare no competing interests.

Acknowledgements

I. A. gratefully acknowledges financial support from the University of Dhaka for conducting this research project. I. A. thankfully extends his courtesy to the Bangladesh Research and Education Network (BdREN) for providing excellent high-performance computational resources. I. A. also acknowledges resource-sharing support from Md. Shafiul Alam and Md. Mosaddek Khan, University of Dhaka. I. A. would like to extend his courtesy to Shirin Akter Jahan and Md. Saiful Quddus, Institute of Glass and Ceramic Research and Testing (IGCRT), Bangladesh Council of Scientific and Industrial Research (BCSIR) for facilitating XPS measurements. K. S. H. acknowledges the support from the International Science Program (ISP), Uppsala University, Sweden. T. A. M. acknowledges a Research Fellowship from the Semiconductor Technology Research Centre, University of Dhaka.

References

1 P. Chen, H. Liu, W. Cui, S. C. Lee, L. Wang and F. Dong, *EcoMat*, 2020, **2**, e12047.
2 W. Fang and W. Shangguan, *Int. J. Hydrogen Energy*, 2019, **44**, 895.
3 R. He, D. Xu, B. Cheng, J. Yu and W. Ho, *Nanoscale Horiz.*, 2018, **3**, 464.
4 S. Wang, L. Wang and W. Huang, *J. Mater. Chem. A*, 2020, **8**, 24307.
5 R. Yu, A. Fan, M. Yuan, T. Li and J. Wang, *Phys. Chem. Chem. Phys.*, 2016, **18**, 23702.

6 Q. Sun, J. Wang, W.-J. Yin and Y. Yan, *Adv. Mater.*, 2018, **30**, 1705901.
7 D. Tiwari, D. Alibhai, D. Cherns and D. J. Fermin, *Chem. Mater.*, 2020, **32**, 1235.
8 K. Yoshii, T. Fukuda, H. Akahama, J. Kano, T. Kambe and N. Ikeda, *Phys. C*, 2011, **471**, 766.
9 I. M. Szilágyi, B. Fórizs, O. Rosseler, Á. Szegedi, P. Németh, P. Király, G. Tárkányi, B. Vajna, K. Varga-Josepovits, K. László, *et al.*, *J. Catal.*, 2012, **294**, 119.
10 F. Wang, C. Di Valentin and G. Pacchioni, *J. Phys. Chem. C*, 2012, **116**, 8901.
11 V. Dutta, S. Sharma, P. Raizada, V. K. Thakur, A. A. P. Khan, V. Saini, A. M. Asiri and P. Singh, *J. Environ. Chem. Eng.*, 2021, **9**, 105018.
12 X. Liu, S. Gu, Y. Zhao, G. Zhou and W. Li, *J. Mater. Sci. Technol.*, 2020, **56**, 45.
13 J. Tian, Y. Sang, G. Yu, H. Jiang, X. Mu and H. Liu, *Adv. Mater.*, 2013, **25**, 5075.
14 A. Elaouni, M. El Ouardi, A. BaQais, M. Arab, M. Saadi and H. A. Ahsaine, *RSC Adv.*, 2023, **13**, 17476.
15 H. Yi, L. Qin, D. Huang, G. Zeng, C. Lai, X. Liu, B. Li, H. Wang, C. Zhou, F. Huang, S. Liu and X. Guo, *Chem. Eng. J.*, 2019, **358**, 480.
16 Q. S. Hossain, S. Ahmed, S. S. Nishat, M. Z. Hossain, M. Khan, T. Hasan, M. S. Bashar, M. Hakim, I. M. Syed, K. S. Hossain and I. Ahmed, *RSC Adv.*, 2023, **13**, 14291.
17 M. Z. Hossain, S. S. Nishat, S. Ahmed, Q. S. Hossain, M. Khan, T. Hasan, M. S. Bashar, A. S. H. Faysal, I. M. Syed, K. S. Hossain, S. Hussain, M. M. Khan and I. Ahmed, *RSC Adv.*, 2023, **13**, 5576.
18 X. Liu and H.-Q. Fan, *Optik*, 2018, **158**, 962.
19 T. P. T. Linh, N. D. Phu, P. Van Hai and L. H. Hoang, *J. Electron. Mater.*, 2021, **50**, 4027.
20 J. Tao, Q. Zhang and T. Liu, *Phys. Chem. Chem. Phys.*, 2022, **24**, 22918.
21 A. Rauf, M. Ma, S. Kim, M. S. A. S. Shah, C.-H. Chung, J. H. Park and P. J. Yoo, *Nanoscale*, 2018, **10**, 3026.
22 X. Meng and Z. Zhang, *J. Photochem. Photobiol., A*, 2015, **310**, 33.
23 J. Zhang, P. Deng, M. Deng, H. Shen, Z. Feng and H. Li, *ACS Omega*, 2020, **5**, 29081.
24 H. Ahmad, A. Rauf, A. Ahmad, A. Ulhaq and S. Muhammad, *RSC Adv.*, 2021, **11**, 32330.
25 N. N. Lathiotakis, A. N. Andriotis and M. Menon, *Phys. Rev. B: Condens. Matter Mater. Phys.*, 2008, **78**, 193311.
26 S.-G. Park, B. Magyari-Köpe and Y. Nishi, *Phys. Rev. B: Condens. Matter Mater. Phys.*, 2010, **82**, 115109.
27 G. Kresse and J. Furthmüller, *Phys. Rev. B: Condens. Matter Mater. Phys.*, 1996, **54**, 11169.
28 G. Kresse and D. Joubert, *Phys. Rev. B: Condens. Matter Mater. Phys.*, 1999, **59**, 1758.
29 A. Jain, Y. Shin and K. A. Persson, *Nat. Rev. Mater.*, 2016, **1**, 1.
30 R. O. Jones, *Rev. Mod. Phys.*, 2015, **87**, 897.
31 P. Giannozzi, S. Baroni, N. Bonini, M. Calandra, R. Car, C. Cavazzoni, D. Ceresoli, G. L. Chiarotti, M. Cococcioni, I. Dabo, *et al.*, *J. Phys.: Condens. Matter*, 2009, **21**, 395502.
32 P. Giannozzi, O. Andreussi, T. Brumme, O. Bunau, M. B. Nardelli, M. Calandra, R. Car, C. Cavazzoni, D. Ceresoli, M. Cococcioni, *et al.*, *J. Phys.: Condens.Matter*, 2017, **29**, 465901.
33 P. Giannozzi, O. Baseggio, P. Bonfà, D. Brunato, R. Car, I. Carnimeo, C. Cavazzoni, S. De Gironcoli, P. Delugas, F. Ferrari Ruffino, *et al.*, *J. Chem. Phys.*, 2020, **152**, 154105.
34 D. M. Ceperley and B. J. Alder, *Phys. Rev. Lett.*, 1980, **45**, 566.
35 G. B. Bachelet, D. R. Hamann and M. Schlüter, *Phys. Rev. B: Condens. Matter Mater. Phys.*, 1982, **26**, 4199.
36 M. Bettega, L. Ferreira and M. Lima, *Phys. Rev. A*, 1993, **47**, 1111.
37 G. Kresse and J. Hafner, *J. Condens. Matter Phys.*, 1994, **6**, 8245.
38 J. Fardush Tanha, S. Farhad, U. Honey, N. Tanvir, T. Hasan, S. Shahriyar Nishat, A. Kabir, S. Ahmed, M. Hakim, M. Khan, M. Moniruzzaman and I. Ahmed, *J. Appl. Phys.*, 2021, **130**, 235107.
39 S. Ahmed, S. S. Nishat, A. Kabir, A. S. H. Faysal, T. Hasan, S. Chakraborty and I. Ahmed, *Phys. B*, 2021, **615**, 413061.
40 S. Ahmed, T. Hasan, A. S. H. Faysal, S. S. Nishat, M. Khan, A. Kabir and I. Ahmed, *Comput. Mater. Sci.*, 2022, **214**, 111743.
41 X. Ma, B. Lu, D. Li, R. Shi, C. Pan and Y. Zhu, *J. Phys. Chem. C*, 2011, **115**, 4680.
42 H. S. Park, K. E. Kweon, H. Ye, E. Paek, G. S. Hwang and A. J. Bard, *J. Phys. Chem. C*, 2011, **115**, 17870.
43 O. Volnianska, P. Boguslawski, J. Kaczkowski, P. Jakubas, A. Jezierski and E. Kaminska, *Phys. Rev. B: Condens. Matter Mater. Phys.*, 2009, **80**, 245212.
44 R. M. Sheetz, I. Ponomareva, E. Richter, A. N. Andriotis and M. Menon, *Phys. Rev. B: Condens. Matter Mater. Phys.*, 2009, **80**, 195314.
45 S. Grimme, S. Ehrlich and L. Goerigk, *J. Comput. Chem.*, 2011, **32**, 1456.
46 A. Togo and I. Tanaka, *Scr. Mater.*, 2015, **108**, 1.
47 A. Togo, L. Chaput, T. Tadano and I. Tanaka, *J. Phys.: Condens. Matter*, 2023, **35**(35), 353001.
48 T. Le Bahers, M. Rerat and P. Sautet, *J. Phys. Chem. C*, 2014, **118**, 5997.
49 C. Franchini, *J. Phys.: Condens.Matter*, 2014, **26**, 253202.
50 A. Stroppa and G. Kresse, *Phys. Rev. B: Condens. Matter Mater. Phys.*, 2009, **79**, 201201.
51 A. Stroppa and S. Picozzi, *Phys. Chem. Chem. Phys.*, 2010, **12**, 5405.
52 M. Marsman, J. Paier, A. Stroppa and G. Kresse, *J. Phys.: Condens.Matter*, 2008, **20**, 064201.
53 K. E. Kweon and G. S. Hwang, *Phys. Rev. B: Condens. Matter Mater. Phys.*, 2012, **86**, 165209.
54 A. D. Becke, *J. Chem. Phys.*, 1993, **98**, 1372.
55 J. Paier, M. Marsman and G. Kresse, *Phys. Rev. B: Condens. Matter Mater. Phys.*, 2008, **78**, 121201.
56 K. E. Kweon and G. S. Hwang, *Phys. Rev. B: Condens. Matter Mater. Phys.*, 2013, **87**, 205202.
57 A. A. Mostofi, J. R. Yates, Y.-S. Lee, I. Souza, D. Vanderbilt and N. Marzari, *Comput. Phys. Commun.*, 2008, **178**, 685.
58 Y. Hou, S. Ardo and R. Wu, *Phys. Rev. Mater.*, 2021, **5**, 065801.

59 S. Ahmed, A. S. H. Faysal, M. Khan, M. Basith, M. S. Bashar, H. Das, T. Hasan and I. Ahmed, *Results Phys.*, 2021, **31**, 104940.
60 T. Hasan, A. Saha, M. Khan, R. Rashid, M. Basith, M. S. Bashar and I. Ahmed, *AIP Adv.*, 2022, **12**(9), 095003.
61 T. Zeng, X. Yu, S. Hui, Z. Zhou and X. Dong, *Mater. Res. Bull.*, 2015, **68**, 271.
62 M. Maczka, J. Hanuza, W. Paraguassu, G. Souza Filho, P. Tarso Cavalcante Freire, J. Mendes Filho, *et al.*, *Appl. Phys. Lett.*, 2008, **92**, 112911.
63 K. Zhou, J. Lu, Y. Yan, C. Zhang, Y. Qiu and W. Li, *RSC Adv.*, 2020, **10**, 12068.
64 M. Ge and L. Liu, *Mater. Sci. Semicond. Process.*, 2014, **25**, 258.
65 L.-W. Zhang, Y.-J. Wang, H.-Y. Cheng, W.-Q. Yao and Y.-F. Zhu, *Adv. Mater.*, 2009, **21**, 1286.
66 J. Yu, J. Xiong, B. Cheng, Y. Yu and J. Wang, *J. Solid State Chem.*, 2005, **178**, 1968.
67 F. Chen, D. Li, B. Luo, M. Chen and W. Shi, *J. Alloys Compd.*, 2017, **694**, 193.
68 R. Song, N. Chen, B. Han, S. Yu, Y. Wang, K. Liu, Z. Tong and H. Zhang, *Environ. Sci. Pollut. Res.*, 2021, **28**, 36434.
69 Y.-H. B. Liao, J. X. Wang, J.-S. Lin, W.-H. Chung, W.-Y. Lin and C.-C. Chen, *Catal. Today*, 2011, **174**, 148.
70 S.-P. Hu, C.-Y. Xu and L. Zhen, *Mater. Lett.*, 2013, **95**, 117.
71 Z. Cui, D. Zeng, T. Tang, J. Liu and C. Xie, *J. Hazard. Mater.*, 2010, **183**, 211.
72 A. Hao, X. Ning, Y. Cao, J. Xie and D. Jia, *Mater. Chem. Front.*, 2020, **4**, 2096.
73 M. T. L. Lai, C. W. Lai, K. M. Lee, S. W. Chook, T. C. K. Yang, S. H. Chong and J. C. Juan, *J. Alloys Compd.*, 2019, **801**, 502.
74 X. Guo, D. Wu, X. Long, Z. Zhang, F. Wang, G. Ai and X. Liu, *Mater. Charact.*, 2020, **163**, 110297.
75 C. Huang, L. Chen, H. Li, Y. Mu and Z. Yang, *RSC Adv.*, 2019, **9**, 27768.
76 A. Pancielejko, J. Łuczak, W. Lisowski, G. Trykowski, D. Venieri, A. Zaleska-Medynska and P. Mazierski, *Appl. Surf. Sci.*, 2022, **599**, 153971.
77 T. Xie, Y. Liu, H. Wang and Z. Wu, *Sci. Rep.*, 2019, **9**, 7551.
78 M. Cheng, L. Yang, H. Li, W. Bai, C. Xiao and Y. Xie, *Nano Res.*, 2021, **14**, 3365.
79 Y. Zhu, Y. Wang, Q. Ling and Y. Zhu, *Appl. Catal., B*, 2017, **200**, 222.
80 X. Wu, D. Vanderbilt and D. Hamann, *Phys. Rev. B: Condens. Matter Mater. Phys.*, 2005, **72**, 035105.
81 S. Shang, Y. Wang and Z.-K. Liu, *Appl. Phys. Lett.*, 2007, **90**, 101909.
82 F. Mouhat and F.-X. Coudert, *Phys. Rev. B: Condens. Matter Mater. Phys.*, 2014, **90**, 224104.
83 Y. Huang, Y. Yuan, F. Ma, Z. Zhang, X. Wei and G. Zhu, *Phys. Status Solidi*, 2018, **255**, 1700653.
84 O. Gomis, B. Lavina, P. Rodríguez-Hernández, A. Muñoz, R. Errandonea, D. Errandonea and M. Bettinelli, *J. Phys.: Condens.Matter*, 2017, **29**, 095401.
85 R. Hill, *Proc. Phys. Soc., London, Sect. A*, 1952, **65**, 349.
86 H. Dong, C. Chen, S. Wang, W. Duan and J. Li, *Appl. Phys. Lett.*, 2013, **102**, 182905.
87 M. Yaakob, M. Taib, M. Deni, A. Chandra, L. Lu and M. Yahya, *Ceram. Int.*, 2013, **39**, S283.
88 K. B. Spooner, A. M. Ganose, W. W. Leung, J. Buckeridge, B. A. Williamson, R. G. Palgrave and D. O. Scanlon, *Chem. Mater.*, 2021, **33**, 7441.
89 Y. Tsuji, P. L. Dasari, S. Elatresh, R. Hoffmann and N. Ashcroft, *J. Am. Chem. Soc.*, 2016, **138**, 14108.